Asymmetry and global instability of real minivans' wake

G. Bonnavion[a], O. Cadot[b,*], V. Herbert[c], S. Parpais[d], R. Vigneron[e], J. Délery[e]

[a] *IMSIA, ENSTA-ParisTech, UMR 9219 CNRS, 828 Boulevard des Maréchaux, 91762 Palaiseau Cedex, France*
[b] *University of Liverpool, School of Engineering, Liverpool L69 BX7, United Kingdom*
[c] *Groupe PSA, Route de Gisy, 78140 Vélizy-Villacoublay, France*
[d] *Groupe Renault, 1 avenue du Golf, 78280 Guyancourt, France*
[e] *GIE-S2A, 2 Avenue Volta, 78180 Montigny-le-Bretonneux, France*

Abstract

Three real minivan cars are investigated through base pressure distribution, force balance and velocity measurements. Discontinuous transitions of permanent wake reversals and bistable dynamics between two well-defined states are observed varying ground clearance, pitch and yaw, with open and closed air-intake. These transitions prove that the cars undergo the same global z-instability as the square-back Ahmed body (M. Grandemange, M. Gohlke and O. Cadot, Physics of Fluids, **25**, 2013). The contribution of the global instability to the lift coefficient is estimated to 0.012 and 0.024 depending on the wake state. Eventually, a demonstrative experiment of a real minivan drag reduction is shown to be improved by a factor 2 with a direct passive control of the z-instability.

Keywords: turbulent flow, bluff body, cars aerodynamics, wake multistability, bistability, static asymmetric modes

1. Introduction

From the aerodynamics point of view, minivan cars are bluff bodies with vertical blunt rear geometry responsible for a massive flow separation leading to a turbulent recirculation and a wide wake. For a better understanding of the flow physics aiming at improving their aerodynamic performances, simplified models such as the Ahmed squareback body [1] have been extensively studied over the last decades. The seeding work of [2, 3] showed the presence of static asymmetric states of the wake that permanently break the reflectional symmetry of the body. These states have been firmly confirmed since by numerous research teams working on squareback academic bodies both experimentally [4, 5, 6, 7, 8, 9, 10] and numerically [11, 12, 13]. These asymmetric wake states are reminiscent of a global steady instability that appears for a critical Reynolds number through a pitchfork bifurcation in the laminar regime [2, 13]. At the critical Reynolds number (few hundreds), the basic flow

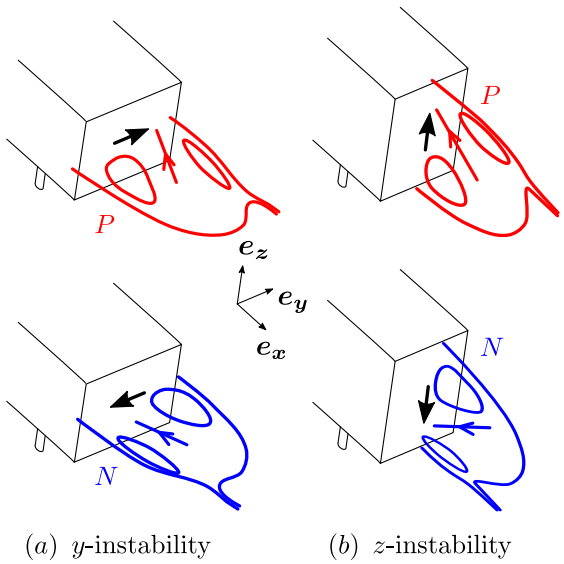

(a) y-instability (b) z-instability

Figure 1: Sketches of the recirculating bubbles for the y-instability (a) and z-instability (b) interpreted from the mean wake measurements of [14]. Thick arrows display the corresponding base pressure gradients defining the P (positive) or N (negative) state depending on its sign.

*Corresponding author
Email address: Olivier.Cadot@liverpool.ac.uk (O. Cadot)

that respects all the symmetries becomes unstable (i.e. not observable), and the two asymmetric states become steadily stable. These P and N states are illustrated in figure $1(a)$. Depending on the initial flow conditions and the residual imperfections, only one state is selected in the laminar regime. As the Reynolds number is increased and the flow becomes turbulent, the reflectional symmetry is statistically restored through bistable long-time dynamics [3, 4] consisting in random switching between state P and state N. These states have been observed for the Ahmed body from the laminar regime at Re= 340 [2, 13] to the industrial flow scale at Re= 2.5×10^6 with rotating wheels and road effect [15].

As reported in [14, 16], there is a critical ground clearance c_c^* below which a stabilization effect occurs: the asymmetric states are suppressed and the reflectionnal symmetry is restored. This ground clearance is approximately $c_c^* \approx 0.1W$ at the Reynolds number $\mathrm{Re}_W = 4.5 \times 10^4$ based on the body width W [14]. For increasing Reynolds numbers, the critical ground clearance decreases continuously as $\mathrm{Re}_W^{-1/6}$ [16]. Hence, sufficient flow at the bottom edge of the base is actually necessary for the global wake instability. A similar conclusion was reported by [17] changing the under-body porosity keeping a constant ground clearance. For real minivan cars, the ground clearance is always high enough (i.e. $c_c^* > 0.1W$) to not have to consider any stabilization effects due to large under-body flow rate deficit.

Later, [14] showed the importance of the rectangular base aspect ratio that can trigger either left/right asymmetric states when the base is wider than it is tall or top/bottom asymmetric states when the base is taller than it is wide. They are respectively called y- and z-instabilities, where y and z refer to the wake asymmetry directions as depicted in figure 1. Although the y-instability corresponds to a pure reflectionnal symmetry-breaking, the z-instability does not, because of the ground and the body supports [14]. The consequence is that the z-instability in the turbulent regime has no reason to lead to bistable dynamics, since there is no symmetry to restore unlike for the y-instability. Hence, it is not an easy task to diagnose a z-instability, since in the absence of a bistable dynamics, the permanent vertical wake asymmetry can be legitimately ascribed to the car top/bottom asymmetrical shape and ground proximity. Apart from the study of [14], there are only few studies [18, 19] of the z-instability.

Beside, the only case of bistable dynamics of a real minivan car reported in the literature with a Renault Kangoo [20] showed huge fluctuations of lift between two most probable values for the car in yaw at 4°. This case was deeply characterized in [21] who also mentioned the importance of the flow through the air-intake. They interpreted these bistable dynamics to be caused by the z-instability.

A clear diagnosis of z-instability was recently presented in [19] for a flat-backed Ahmed body. In the presence of the instability, the vertical component of the base pressure gradient (and lift) undergoes discontinuous transitions when pitch, yaw and ground clearance are varied. At each transition, the dynamics is bistable due to a symmetry compensation effect in the z-direction, basically related to an intensity modification of the under-body flow. In yaw, this change is produced by the wake of the front leeward wheel. In addition, the authors propose a relationship between the cross-flow coefficients and the base pressure gradient components involving an explicit contribution of the global instability strength.

The aim of this paper is to make use of the same strategy of [19] to prove that the wakes of the real cars at full flow scale; the Peugeot 5008, the Peugeot Partner, the Citroën Berlingo and the Renault Kangoo [20, 21] are permanently subjected to a z-instability. To illustrate the impact of the global instability on the aerodynamics performance, a passive control of the instability is achieved for an improved drag reduction of the Peugeot Partner.

The paper is organized as follows. The experimental setup is described in § 2. Results in § 3 are split into four parts, § 3.1 presents the baselines characteristics, § 3.2 investigates the wake response to variations of ground clearance, pitch and yaw angles, § 3.3 assesses the global instability contribution to the aerodynamics force and § 3.4 evidences a beneficial impact of controlling the instability. Finally, a concluding discussion § 4 ends the paper.

2. Experiments

2.1. Wind tunnel and minivan models

The experiments are conducted in the full-scale wind tunnel of the GIE-S2A (*Soufflerie Aéroacoustiques Automobiles*, Montigny-le-Bretonneux, France) dedicated to ground vehicles' aerodynamics. A full description of the facility can

be found in [22]. Among the main characteristics, the test section is a 3/4-open jet. A rolling belt moving at the air-speed between the wheels mimics the road and four wheel-spinners simulate realistic driving conditions. The boundary layer is controlled by suction upstream of the vehicle.

Three blunt based vehicles are considered in this study: a Peugeot 5008 (figure 2a), a Peugeot Partner (figure 2b) and a Citroën Berlingo (figure 2c). The characteristic dimensions of the vehicles can be found in table 1 in which the Renault Kangoo studied in [20, 21] is also mentioned.

The ground proximity is adjusted owing four vertical hydraulic cylinders fixed to the car underbody near each wheel and to the force balance. The car can be independently pushed-up or pulled-down near each axle. The minimum and maximum heights are limited by the springs of the car suspension system. The ground proximity is measured by the distances λ_f between the ground and the top of the wheel-arch for the front axle and λ_r for the rear axle as indicated in figure 2(d). A pitch angle α can be computed from these two heights and the wheelbase Λ such that:

$$\tan\alpha = \frac{\lambda_f - \lambda_r}{\Lambda}. \qquad (1)$$

Positive pitch angles correspond to car nose-up and negative to car nose-down (see figure 2d). A large turntable supports the force balance, the moving belt and the car to adjust the yaw angle β (figure 2d).

The base height H and the free-stream velocity U_∞ are chosen as the characteristic dimensions of the problem and any quantities with superscript * are then non-dimensionalized using H and U_∞ (for instance the non dimensional time is $t^* = tU_\infty/H$). The Reynolds number is thus defined as $\mathrm{Re} = \frac{U_\infty H}{\nu}$, ν being the kinematic viscosity of air. Two different free-stream velocities are used for the tests: $U_\infty = 38.9 \pm 0.1$ m.s^{-1} for the Peugeot 5008 and Partner and $U_\infty = 33.3 \pm 0.1$ m.s^{-1} for the Citroën Berlingo. The temperature is regulated at 20°C. In these regimes, the flow non-uniformity of the facility lies below 0.4%.

The vehicles are either tested in real driving conditions with the front air-intake dedicated to the engine and breaks cooling system open, or obstructed to avoid air through the body as for academic Ahmed bodies [1].

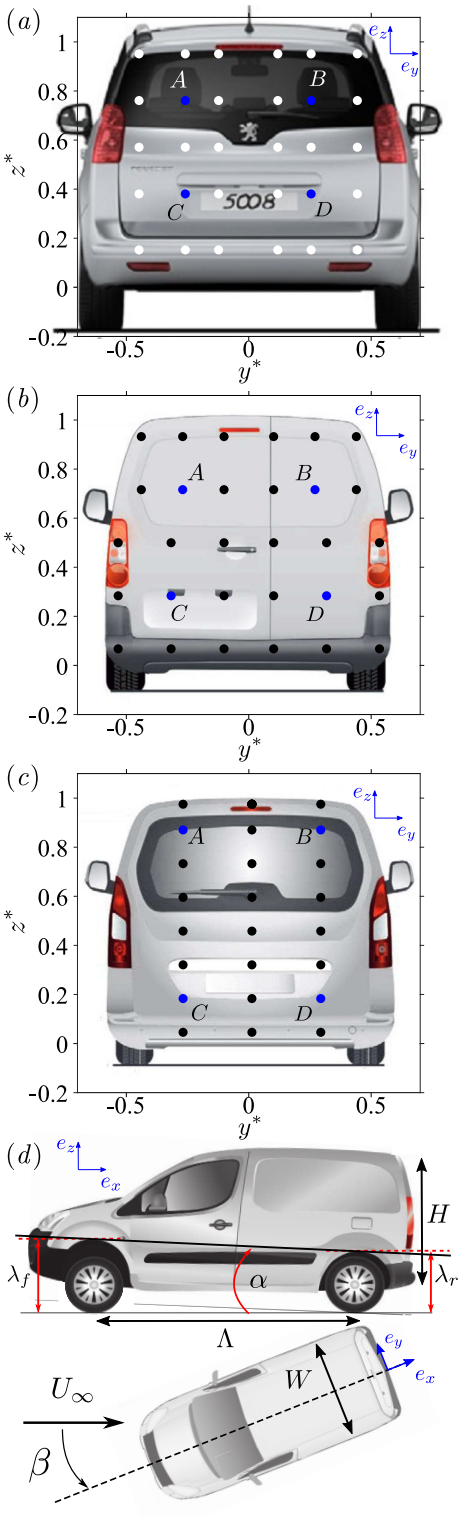

Figure 2: Vehicles with pressure tap locations (filled circles) and geometrical characteristics. (a) Peugeot 5008, (b) Peugeot Partner and (c) Citroën Berlingo. (d) Definition of the distances λ_f, λ_r, pitch angle α and yaw angle β. Lengths are expressed in the non dimensional unit $y^* = y/H$, $z^* = z/H$.

Table 1: Dimensions of the vehicles and flow Reynolds numbers. The superscript * indicates lengths expressed in unit of H. The given values for the front and rear wheel-arch heights are defining the baselines. The Renault Kangoo is reported from [20, 21].

Dimension	5008	Kangoo [20, 21]	Partner	Berlingo
Base height H:	1.320 m	1.480 m	1.480 m	1.480 m
Base aspect ratio or width W^*:	1.212	1.115	1.121	1.121
Vehicle's length L^*:	3.431	2.893	2.959	2.959
Frontal surface S^*:	1.578	1.297	1.297	1.297
Wheelbase Λ^*:	2.114	1.822	1.843	1.843
Front wheel-arch height λ_f^*:	0.519	0.488	0.480	0.480
Rear wheel-arch height λ_r^*:	0.539	0.488	0.480	0.480
Natural pitch angle α:	$-0.55°$	$0°$	$0°$	$0°$
$\mathrm{Re} = \frac{U_\infty H}{\nu}$:	5.13×10^6	4.93×10^6	5.76×10^6	5.13×10^6

2.2. Measurements of wall pressure, aerodynamic force and velocity fields

The vehicle's base pressure distribution is estimated owing to n pressure taps distributed over the car's base (Peugeot 5008, $n = 30$; Peugeot Partner, $n = 30$; Citroën Berlingo, $n = 24$) and connected to a Scanivalve ZOC22b pressure scanner operated with a GLE/SmartZOC100 electronics at a sampling frequency of 200 Hz. The actual cut-off frequency of the pressure measurement due to the vinyl tubing length connecting the pressure tap to the scanner is approximately 20 Hz. Nonetheless, it is sufficient to capture the long-time dynamics of the wake that occur at lower frequencies than few Hertz [20, 21]. The location of the base pressure taps can be found for each of the vehicles in figure $2(a-c)$. The scanner actually gives the differential pressure $p - p_\infty$, where the static pressure p_∞ is obtained from the upstream section of the facility. This differential pressure is expressed as the pressure coefficient :

$$c_p = \frac{p - p_\infty}{\frac{1}{2}\,\rho\,U_\infty^2}, \tag{2}$$

where ρ is the air density.

The instantaneous base suction coefficient c_b is computed from the pressure taps located at the base:

$$c_b = -\frac{1}{n}\sum_{i=1}^{n} c_p(y_i^*, z_i^*) \tag{3}$$

A base pressure gradient $\mathbf{g}^*$ is computed using the taps in blue color and indicated as A, B, C, D in figure $2(a-c)$. The procedure is the same for all vehicles. The two Cartesian components are computed as:

$$g_y^* = \frac{1}{2} \times \left[\frac{c_p(y_B^*, z_B^*) - c_p(y_A^*, z_A^*)}{y_B^* - y_A^*} + \frac{c_p(y_D^*, z_D^*) - c_p(y_C^*, z_C^*)}{y_D^* - y_C^*} \right] \tag{4}$$

and:

$$g_z^* = \frac{1}{2} \times \left[\frac{c_p(y_A^*, z_A^*) - c_p(y_C^*, z_C^*)}{z_A^* - z_C^*} + \frac{c_p(y_B^*, z_B^*) - c_p(y_D^*, z_D^*)}{z_B^* - z_D^*} \right] \tag{5}$$

We use both the Cartesian and polar form of $\mathbf{g}^*$ respectively denoted (g_y^*, g_z^*), referred to as horizontal and vertical gradient components, and (g_r^*, φ), referred to as strength and orientation.

Force measurements are recorded at the sampling frequency of 10 Hz with a six-components force balance provided by Schencker GmbH and located below the wind tunnel floor. The unsteady forces f_x, f_y and f_z, corresponding respectively to drag, side force and lift are made non-dimensional into the coefficients:

$$c_i = \frac{f_i}{\frac{1}{2}\,\rho\,S\,U_\infty^2}, \tag{6}$$

with S being the vehicle's projected frontal area.

Pressure distributions $c_p(y, z, t)$ and force coefficients $c_i(t)$ are simultaneously recorded during $2-4$ minutes. Recorded signals are afterwards low-pass filtered using a sliding window of 0.5 s corresponding to a much lower cut-off frequency than that of

both measurements in order to obtain identical frequency resolution for pressure and force time series. Before each set of experiments, a no-wind acquisition is performed whose averaged value is subtracted to the actual measurements to correct any offset.

Measurements in the wake use three 18-holes spherical probes mounted on a three-axis traversing system [22]. The probes are "omniprobe" models from Aeroprobe Corporation having diameters of 9.53 mm. The measurement is performed continuously at an acquisition rate of 2.5 Hz while the traversing system is moving at a constant speed of 75 mm.s^{-1}. Hence, one measurement point is obtained each 30 mm that sets the spatial resolution. It gives the mean velocities U_x, U_y and U_z and its gradients after processing as well as the static pressure. The uncertainty of the velocity is given by the manufacturer to be less than 1% of the measured velocity modulus, and the angular precision to be less than 0.4°. The automatic displacement allows to get these data in planes iso-x, iso-y or iso-z. In the present experiments, the mean wake is investigated in a vertical plane $y^* = 0$ and displayed as the modulus of the velocity component in that plane, $U^*_{xz} = \sqrt{U^{*2}_x + U^{*2}_z}$ superimposed to the streamlines computed from (U^*_x, U^*_z).

In the following, for any time dependent variable x, capital letter X refers to time averaged value and $X' = \sqrt{(x - X)^2}$ to the mean fluctuations (standard deviation). We recall that superscript * denotes a quantity made non-dimensional using H and U_∞.

3. Results

The results section is organized as follows. We first characterize the baselines flow in § 3.1 for both air intake systems either open or closed. Wake reversals and bistable dynamics are evidenced varying ground clearance in § 3.2.1, pitch angle in § 3.2.2 and yaw angle in § 3.2.3. The strength of the global instability contributing the force coefficient is then investigated in § 3.3 and eventually some demonstrative passive manipulations of the instability is investigated to prove its significant aerodynamic impact in § 3.4.

3.1. Baselines for open and closed air intake

The baseline is defined for the vehicles having their natural wheel-arch heights and pitch angle as given in table 1 and aligned with the incoming flow ($\beta = 0°$). We consider two baseline cases. The first one corresponds to the air-intake system that is not modified so that air can flow through as required by engine cooling. The corresponding mean aerodynamic force coefficient displayed in table 2 shows that all cars with open air intake develop a positive lift coefficient C_z with a negligible side force C_y, never strictly null as a direct consequence of residual asymmetries of the underbodies, engine compartment...

Table 2: Aerodynamics mean coefficients for baseline configurations of the four vehicles with open air-intake. State P (N) stands for mean positive (negative) vertical component of the base pressure gradient as computed in (5).

Vehicle	C_b	C_x	C_y	C_z	State
5008	0.128	0.278	0.003	0.010	P
Kangoo	0.125	0.347	0.004	0.012	P
Partner	0.182	0.339	0.003	0.017	P
Berlingo	0.183	0.336	0.001	0.017	P

Table 3: Aerodynamics mean coefficients for baseline configurations of the four vehicles with closed air-intake. State P (N) stands for mean positive (negative) vertical component of the base pressure gradient as computed in (5).

Vehicle	C_b	C_x	C_y	C_z	State
5008	0.128	0.258	0.002	0.015	P
Kangoo	0.156	0.334	0.004	0.029	N
Partner	0.173	0.318	0.003	0.002	P
Berlingo	0.172	0.312	0.002	0.014	P

For the second case, the front air intake grid at the fore-body is sealed with wide adhesive tape (see illustration in [21]) obliging the flow to go around the body as for academic Ahmed bodies. The closure effect can be seen comparing the aerodynamic force coefficient in table 2 to those obtained in table 3. The closure produces a substantial drag reduction from 7.2% for the 5008, 7.1% for the Berlingo, 6.2% for the Partner down to 3.7% for the Kangoo. These changes are considerable at a vehicle's scale in view of fuel-efficiency and carbon emissions reduction. We can see comparing table 2 to table 3 that the drag reduction is not correlated to the mean base suction C_b. It suggests that the wake is not involved and that the reduction originates

from the large head loss as the air flows through the engine compartment.

The air-intake closure has only little effects on the base pressure distribution of the 5008, the Berlingo and the Partner as shown in figures $3(a, b, c)$ respectively. They all show an almost vertical and positive base pressure gradient with small fluctuations in orientation and modulus as depicted in the probability density functions of figures $3(a, b, c)$. They are well defined states with turbulent fluctuations, with no bi-stable dynamics. We will then qualify the corresponding flows at the base as P states in tables 2 and 3. On the contrary to these cars, the air-intake closure of the Kangoo was observed to produce a permanent wake reversal in [21] from P state to an N state with negative vertical base pressure gradient. This global change of the wake is accompanied by the large increase of lift and base suction in table 3. The wake reversal of the Kangoo is also at the origin of a smaller drag reduction of 3.7% obtained by closing the air-intake than the 6% to 7% of the other cars.

In the following, we aim at revealing hypothetical discontinuous transitions towards a reversed wake state by changing the ground clearance, the pitch and the yaw angles.

3.2. Wake reversals and bistable dynamics

This section presents base pressure gradient responses to variations of the pitch α and the yaw angle β. The responses are assessed as in [19] through the statistics of the base pressure gradient considering each component of coordinate system $(g_y^*,\ g_z^*)$ by representing its probability density function f normalized by its most probable value. The resulting plots are two two-dimensional sensitivity maps for each of the two geometrical configurations varying the parameter $q = \alpha$ or β: $f(q, g_y^*),\ f(q, g_z^*)$. The mean velocity fields of the wake are investigated for chosen specific configurations identified in the sensitivity maps.

3.2.1. Ground clearance variations

The ground clearance experiment is conducted with the Peugeot 5008 only. Since the Ahmed body subjected to the z-instability [14, 19] switches from a P state to a N state when the ground clearance is increased, we simply apply the largest ground clearance accessible to the 5008. The car is then lifted up by 81 mm on each axle from its baseline. The mean base pressure distribution $C_p(y^*, z^*)$ shown in figure $4(a)$ and the base gradient statistics in figures $4(b)$ actually indicates a negative vertical pressure gradient for this highest ground clearance. Unlike for the experiments with the simplified geometry reported in [14, 19], the modulus of the gradient g_r^* is affected by the wake orientation and reduced by almost a factor of two in the N state compared to the P state. A smaller modulus of similar magnitude for the state N was also reported for the Kangoo by [21].

No sensitivity experiments to the ground clearance have been undertaken to investigate the discrete or continuous nature of the transition between the two states. These have been performed in the following changing pitch and yaw.

3.2.2. Pitch variations

Pitch angle sensitivity experiments are conducted with the Peugeot 5008 with open air-intake and Berlingo with closed air-intake. An explored range of $\alpha \in [-0.55°, 1.45°]$ is obtained for the 5008 by changing the rear axle clearance only from the baseline. For the Berlingo, the front wheel-arch is placed at $\lambda_f^* = 0.534$ (80 mm above the baseline defined in table 1) and the rear axle clearance is modified to explore the range $\alpha \in [1.9°, 2.3°]$. The resulting sensitivity maps of the 5008 are given in figure 5, and those of the Berlingo in figure 6. These figures display branches that locate the most probable value of the variable. For both cars, the horizontal component g_y^* in figure $5(a)$ and figure $6(a)$ fluctuates around zero as expected by the reflectional symmetry of the turbulent wake. An unexpected behaviour is observed on the vertical component of the gradient g_z^* in figure $5(b)$ and in figure $6(b)$. The branch observed for low pitches at about $g_z^* \simeq 0.1$ switches as a clear discontinuous transition to a lower branch at about $g_z^* \simeq -0.05$. It is remarkable that the value of each branch keeps an almost constant value independently to the pitch angle variation. These two values define uniquely two states of the wake, the upper branch being the P state and the lower the N state. It is in agreement with the Ahmed body subjected to the z-instability [19] that switches discontinuously from the P state to a N state by increasing positively the pitch angle. Although not reported in this paper, decreasing the pitch from the baseline for the 5008 and Berlingo lead to identical wake state as the baseline.

The mean base pressure distribution $C_p(y^*, z^*)$ of the Peugeot 5008 at the pitch $\alpha = 1.45°$ is shown in figure $7(a)$. It is very similar to the distribution

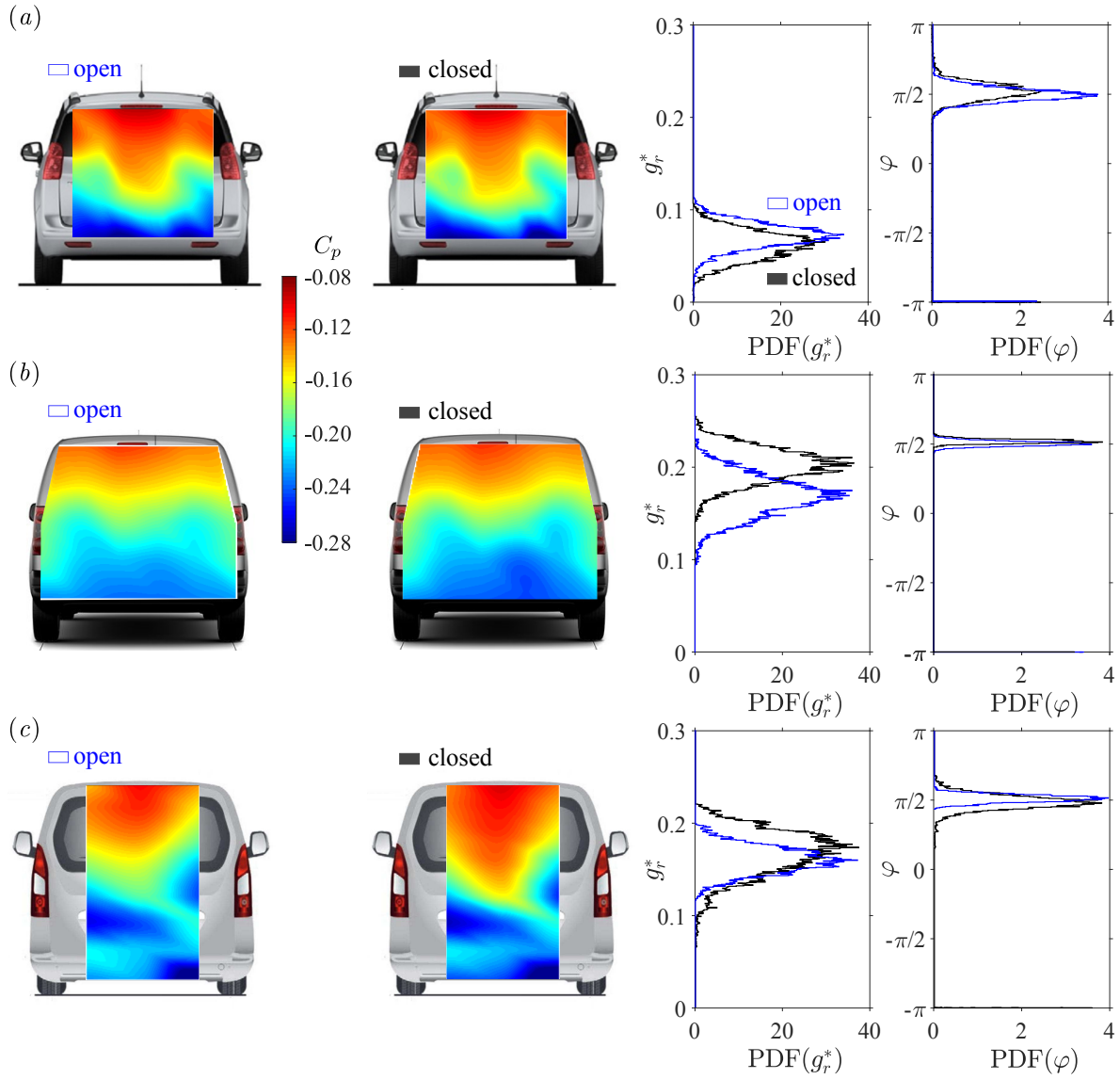

Figure 3: Baselines properties for (a) Peugeot 5008, (b) Peugeot Partner and (c) Citron Berlingo. Mean base pressure distributions $C_p(y^*, z^*)$ with air-intake open (left column) and closed (right column). Corresponding base pressure gradient statistics displayed as modulus (left column) and orientation (right column) for air-intake open (blue line) and closed (black line).

observed with large ground clearance in figure 4(a) since they are both N states. The associated mean wake velocity field is shown in figure 7(b) and compared to the baseline in figure 7(c). With the negative pressure gradient in figure 7(b), the feedback flow in the recirculating bubble is orientated towards the bottom of the car, while it is orientated towards to top of the car for the positive gradient in figure 7(c). Identical observations are made for the Berlingo with closed air-intake in figure 8. The red vertical profile of the pressure coefficient in figure 8(a) indicates a negative vertical gradient for the pitch $\alpha = 2.3°$ while the blue profile shows a positive gradient for the pitch $\alpha = 1.9°$. The associated mean wake velocity field are respectively shown in 8(b) and 8(c). Again, the feedback flow orientation matches the sign of the vertical base pressure gradient indicating the wake reversal. Although the car configuration of the baseline with open air intake has a very different ground clearance, it is shown for comparison in 8(c). It presents the same orientation of the feedback flow as in 8(c)

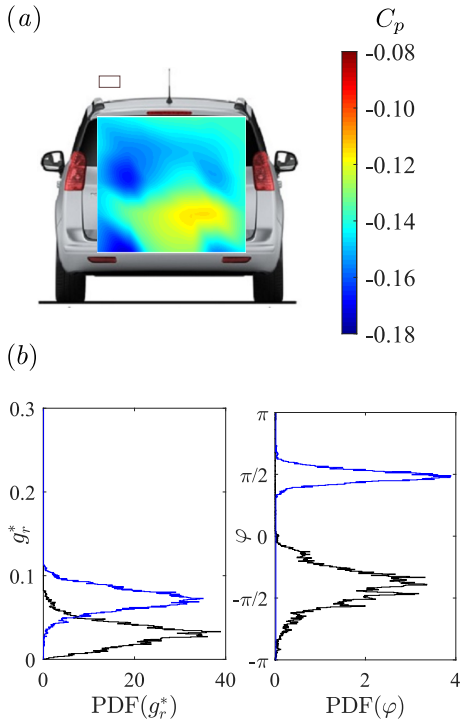

Figure 4: Peugeot 5008 at $\lambda_f^* = 0.580$, $\lambda_r^* = 0.600$ ($\alpha = -0.55°$). Mean base pressure distribution $C_p(y^*, z^*)$ (a). Statistics (b) of the modulus g_r^* and the phase φ of the base pressure gradient. The blue curves in (b) are the corresponding baseline with open air-intake.

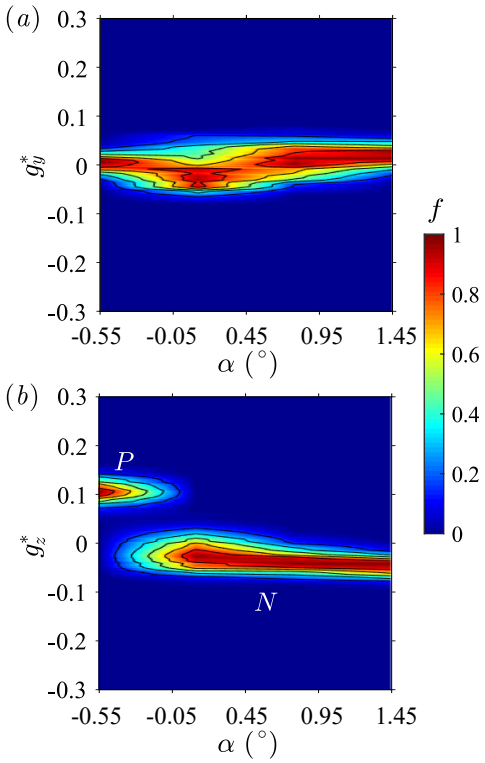

Figure 5: Base pressure gradient response to variations of the pitch angle α for the Peugeot 5008. Sensitivity maps (a) $f(\alpha, g_y^*)$, (b) $f(\alpha, g_z^*)$.

since both are P states, but more surprisingly, the bubble shape of the baseline appears as a mirror symmetry of that of the N state in $8(b)$.

We tried to produce a velocity field at the pitch angle of $\alpha = 2°$, but the measurements were useless due to intermittent switches towards the N state while the traversing probe system was exploring the measurement plane. This sensitivity of the state selection to a body disturbance in the wake is very similar to the work [23] performed with a square-back Ahmed body subjected to the y-instability.

The Partner displayed the same behaviour as the Berlingo in pitch with closed air intake. We also performed pitch experiment for both cars with open air-intake but never observed any wake reversals in that case.

3.2.3. Yaw variations

A yaw angle sensitivity experiment is conducted for the Partner – with closed air-intake – starting from a bi-stable case obtained in pitching conditions with $\alpha = 2.1°, \beta = 0°$ similar to that observed with the Berlingo in figure $6(b)$ during the N to P branch switch at approximately $\alpha = 2.2°$. The response of the base pressure gradient to the yaw variation is given in figure 9. Only positive values of the yaw angle β are considered in view of the quasi-symmetry of the problem.

The yaw produces a small variation of horizontal component of the pressure gradient g_y^* in figure $9(a)$. Nevertheless, the yaw is also able to trigger a discontinuous transition on the vertical component in figure $9(b)$ from the N branch to a P branch. However the most probable gradient of each branch is approximately larger by 30% the value of the 5008 in figure $5(b)$ or the Berlingo in figure $6(b)$. We have no clear explanation for the discrepancy although the Berlingo and the Partner are not strictly identical (differences with the cargo door and the fore-body design), and that the pressure sensors locations are different (figure $2c, d$). Figure 10 shows the mean pressure distributions of the Partner for the yaw $\beta = 1°$. At this yaw, the exploration of the two states (as can be seen in figure $9b$) creates the bistable dynamics. Simple conditional averaging based on the gradient sign gives

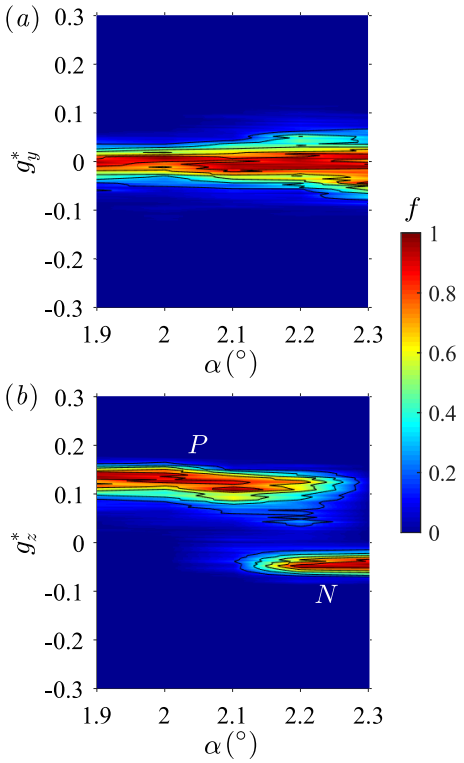

Figure 6: Base pressure gradient response to variations of the pitch angle α for the Berlingo with closed air-intake. Sensitivity maps (a) $f(\alpha, g_y^*)$, (b) $f(\alpha, g_z^*)$.

the mean distribution associated with the P state in figure 10(a) and the N state in figure 10(b). We did not investigate velocity measurements for the yaw experiments.

3.3. Contribution of the z-instability to the aerodynamics force

The relationship between the cross flow force and the base pressure gradient proposed in [19] for a flat blacked Ahmed body subjected to the z-instability will be tested on the data of the Berlingo in pitch (figure 6b) and the Partner in yaw (figure 9b). The relationships read for the side force and lift coefficients :

$$c_y(t^*) = C_y^B - \xi g_y^{*\prime}(t^*) \tag{7a}$$

$$c_z(t^*) = C_z^B - \xi g_z^*(t^*). \tag{7b}$$

For sake of simplicity, we consider the same constant ξ in (7a) and (7b) while it could slightly differs due to the difference in the car shape in the $z-$ and $y-$direction. The two quantities C_y^B and C_z^B are the time independent cross-flow coefficients of the

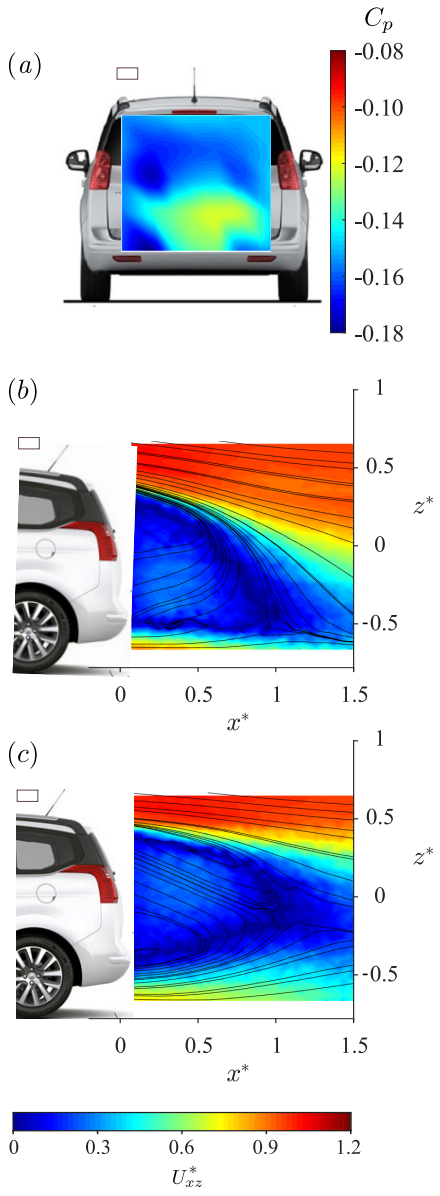

Figure 7: Wake reversals operated by the pitch for the Peugeot 5008. State N at $\alpha = 1.45°$: base pressure coefficient distribution (a), mean velocity field (b). State P at the baseline $\alpha = -0.55°$: mean velocity field (c).

body without the z-instability. They are defining a basic flow assumed to be steady but depending on the pitch and yaw angles. These two force coefficients as well as the constant ξ are obtained by considering the temporal mean of (7):

$$C_y = C_y^B \tag{8a}$$

$$C_z = C_z^B - \xi G_z^* \tag{8b}$$

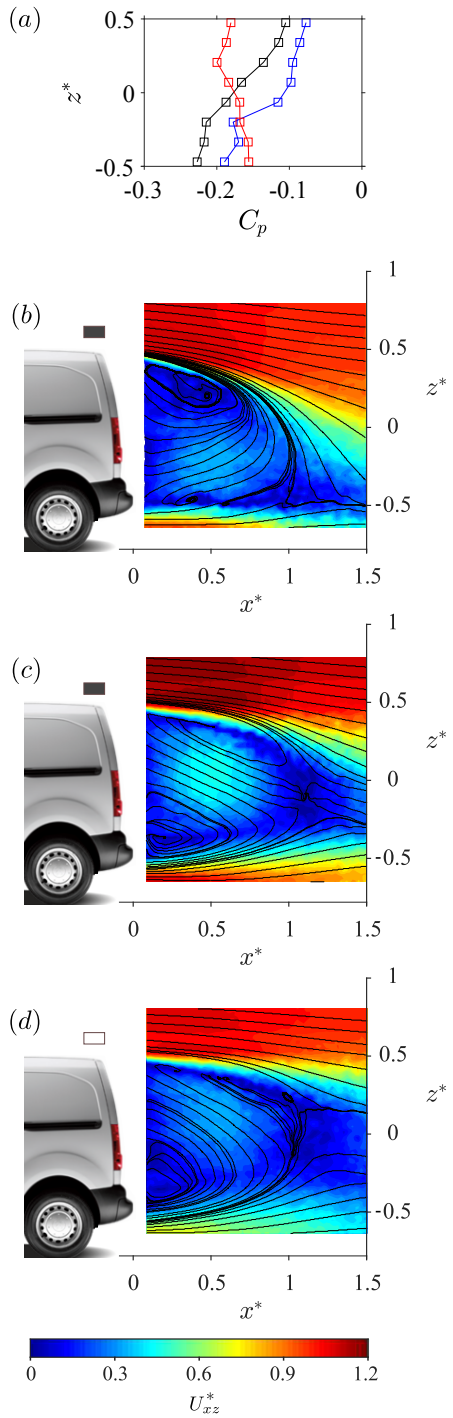

Figure 8: Wake reversals operated by the pitch for the Berlingo. State N with closed air-intake at $\alpha = 2.3°$: base pressure coefficient profile in red curve (a), mean velocity field (b). State P with closed air-intake at $\alpha = 1.9°$: base pressure coefficient profile in blue curve (a), mean velocity field (c). State P at the baseline with open air-intake ($\alpha = 0°$): base pressure coefficient profile in black curve (a), mean velocity field (d).

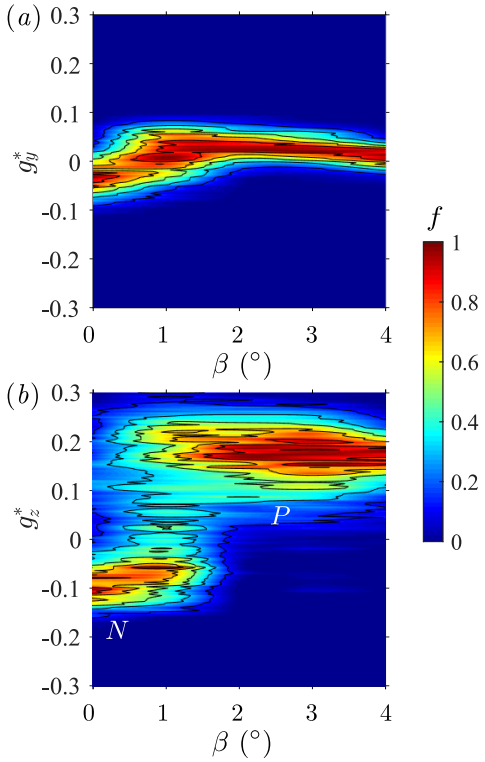

Figure 9: Base pressure gradient response to variations of the yaw angle β for the Partner with closed air-intake. Sensitivity maps (a) $f(\beta, g^*_y)$, (b) $f(\beta, g^*_z)$.

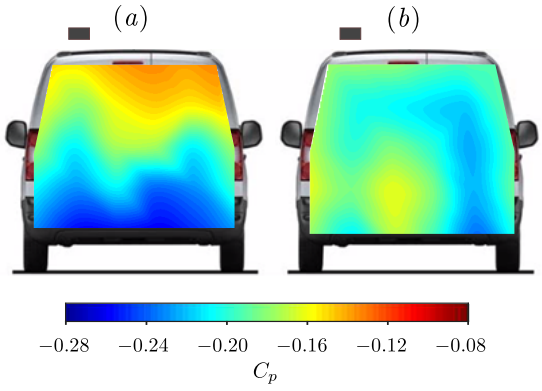

Figure 10: Conditionally averaged mean base pressure distributions $C_p(y^*, z^*)$ (see text) for states P (a) and N (b) of the Partner in yaw at $\beta = 1°$ and with closed air-intake.

Hence, C_y^B is simply given by the mean side force coefficient of the vehicle as a result of the matching mechanism of the z-instability reported in [19]. The lift coefficient C_z^B of the basic flow and the constant ξ are obtained with a best fit involving the measurements of the mean lift C_z and mean vertical component of the base pressure gradient G^*_z.

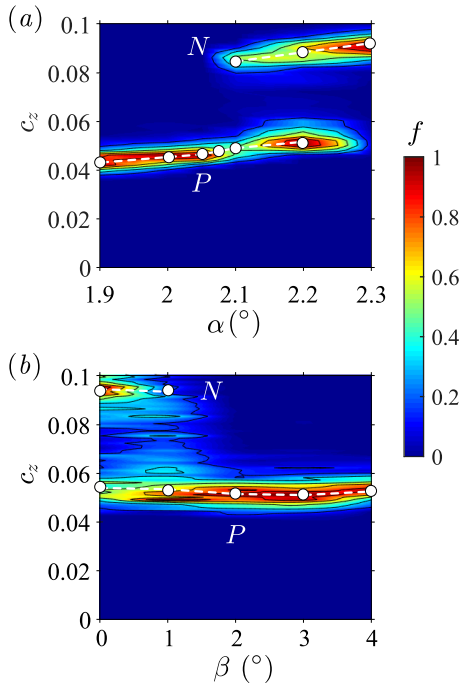

Figure 11: Lift coefficient response c_z of the Berlingo (a) to variations of the pitch angle α with closed air intake and of the Partner (b) to variations of the yaw angle β with closed air-intake. Circle symbols are conditional averaging based on the sign of the vertical component of the base pressure gradient.

The sensitivity maps of the lift coefficient are shown in figure 11(a) for the Berlingo in pitch and in figure 11(b) for the Partner in yaw. The two branches P and N are easily identifiable and extractable by computing the conditional averaging (displayed with symbols) based on the simultaneous sign of the vertical component of the pressure gradient. Because a positive (respectively negative) vertical component of the base pressure gradient is associated with a negative (respectively positive) vertical component of the force, the upper branch having larger lift corresponds to N states and the lower branch to P states.

The mean force coefficients of the vehicles are shown as filled black circles for the Berlingo in pitch in figure 12(a,b) and the Partner in yaw in figure 13(a,b). The N and P branches of c_z in thick black lines in figures 12(b) and 13(b) are extracted for clarity from the sensitivity maps as shown in figure 11. In figure 12(b), C_z^B is assumed to be affine with α and the best fit gives:

$$C_z^B = 0.052\alpha - 0.036. \tag{9}$$

with $\xi = 1/5.3$. In figure 13(b), C_z^B is assumed to be quadratic with β (to respect the symmetry $\beta \to -\beta$) and the best fit gives:

$$C_z^B = 4 \times 10^{-4}\beta^2 + 0.078 \tag{10}$$

with $\xi = 1/6.5$. In both relations (9) and (10), angles are expressed in degrees. Using the results of the fits, the mean relationship (7b) is plotted as the blue dashed lines in both figures 12(b) and 13(b), which satisfactorily matches the mean lift measurements. The mean fluctuation measurements C_y' and C_z' are also well recovered in figures 12(c,d) and 13(c,d) by the relation (7) yielding to:

$$C_y{}' = \xi G_y^{*\prime} \tag{11a}$$

$$C_z{}' = \xi G_z^{*\prime} \tag{11b}$$

Eventually, the time series of the measured instantaneous lift coefficient is compared to the model (7b) computed from the pressure gradient time-series using the basic flow coefficient and ξ found above. The comparison is shown in figure 14 during both bi-stable dynamics at $\alpha = 2.2^\circ$ for the Berlingo and $\beta = 1^\circ$ for the Partner. In conclusion, the relationship (7b) deduced from the flat backed Ahmed bodies [19] is indeed well checked for a complex real geometry at a real flow scale. In addition, the contribution of the z-instability to the lift force coefficient is similar for both cars; it is estimated from the difference between the basic flow coefficient and the P and N branches in both figures 12(b) and 13(b). It approximately corresponds to substantial coefficient lift strengths of 0.012 for the N state, and 0.024 for the P state. To give an idea, they respectively represent about 3.5% and 7% of the drag or 70% and 140% of the lift of the baseline with open air-intake.

Figure 15 shows the evolution of the mean drag coefficient during both pitch and yaw sensitivity experiments. In the case of the flat backed body [19], the mean drag reaches a minimum at each transitions where the bistable dynamics occur (i.e. where the wake fluctuations are the largest) for both the y- and z-instabilities. The explanation given in [5] being that switching events of the bistable dynamics have lower drag that the asymmetric states. This effect seems to be retrieve in figure 15 for real cars where minima can be found around both transitions at $\alpha \approx 2.2^\circ$ in pitch and $\beta \approx 1^\circ$ in yaw. Independently to this effect, conditional averaging operated on P or N state reveals different drags, with larger

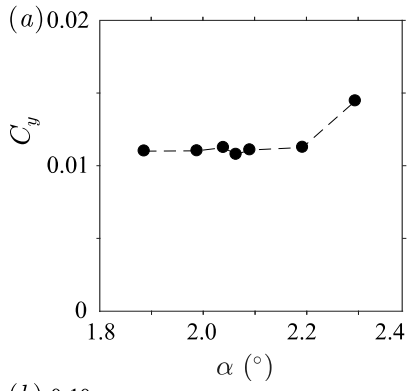

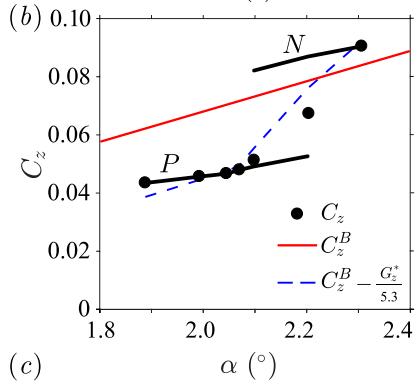

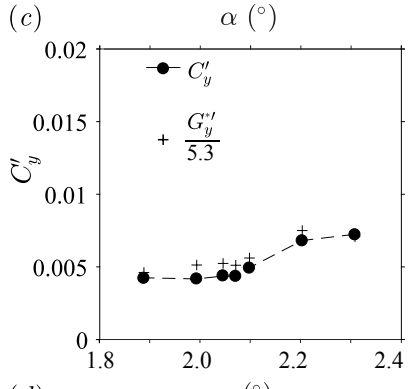

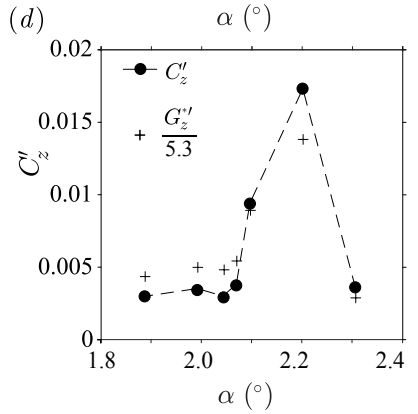

Figure 12: Pitch sensitivity analysis for the Berlingo: (a) mean side force coefficient, (b) mean (symbols) and branches P and N (thick black lines) reported from figure 11(a), *basic flow* lift coefficient C_z^B (red line) and mean lift computed from equation (7b) in blue dashed line. Mean fluctuation of (c) side force compared to horizontal pressure gradient, (d) lift compared to vertical base pressure gradient.

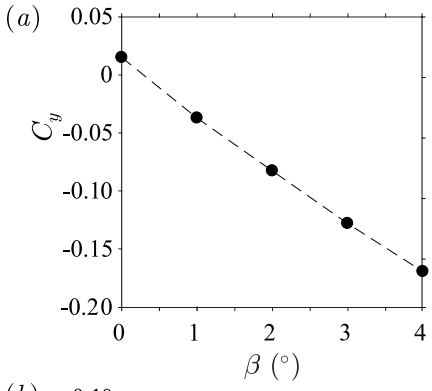

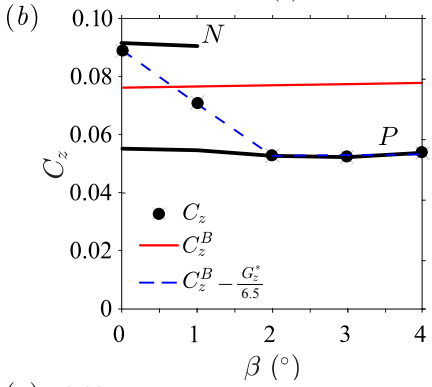

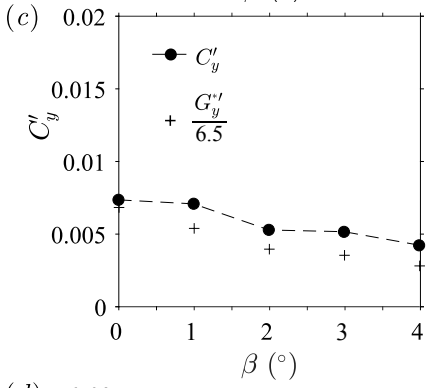

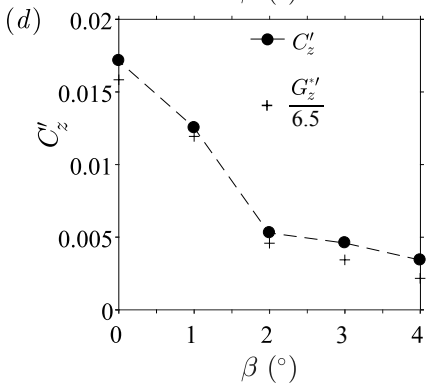

Figure 13: Yaw sensitivity analysis for the Partner: (a) mean side force coefficient, (b) mean (symbols) and branches P and N (thick black lines) reported from figure 11(b), *basic flow* lift coefficient C_z^B (red line) and mean lift computed from equation (7b) in blue dashed line. Mean fluctuation of (c) side force compared to horizontal pressure gradient, (d) lift compared to vertical base pressure gradient.

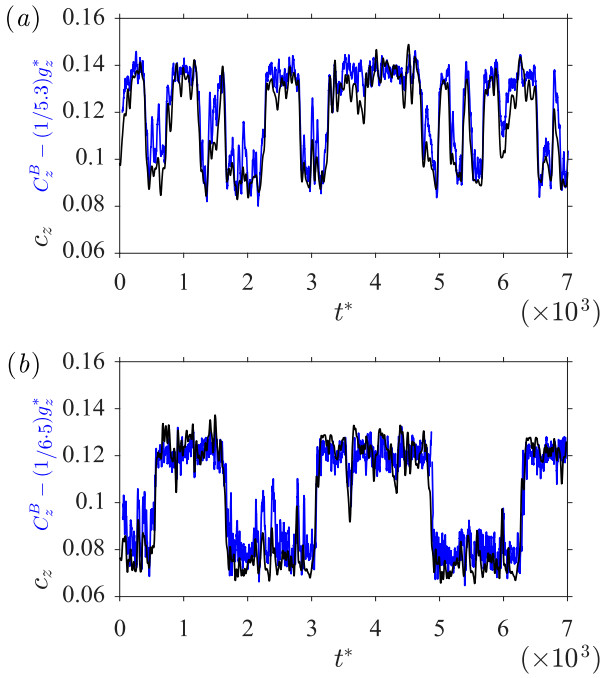

Figure 14: Time series of the lift coefficient $c_z(t^*)$ and reconstructed value from equation (7b) (see text) during bistable dynamics of the Berlingo with closed air-intake in pitch at $\alpha = 2.2°$ (a) and the Partner with closed air-intake in yaw at $\beta = 1°$ (b).

drag for the N state than for the P state. This difference was actually observable in the baselines of the Kangoo car whose drag is given in tables 2 and 3 for open and closed air-intake. While the other cars that remained in a P state with closed air intake show almost no variation or small base suction reduction, the Kangoo base suction increases from $C_b = 0.125$ to $C_b = 0.156$ due to the switch from a P state to a N state. There could be a practical interest to restore the P state for the closed air-intake configuration to further improve the 3.7% of drag reduction of the Kangoo. This practical test is investigated in the following as a demonstration of the beneficial impact of controlling the z-instability.

3.4. Manipulation of the z-instability

A global trend is highlighted above: closing the air-intake is an efficient drag reduction technique – applicable in real driving conditions when the need for engine cooling is low – but would potentially trigger the reversed state N. The state N has poor aerodynamic performance compared to the P state with both a higher base suction increasing drag and a higher lift reducing the vehicle's stability, espe-

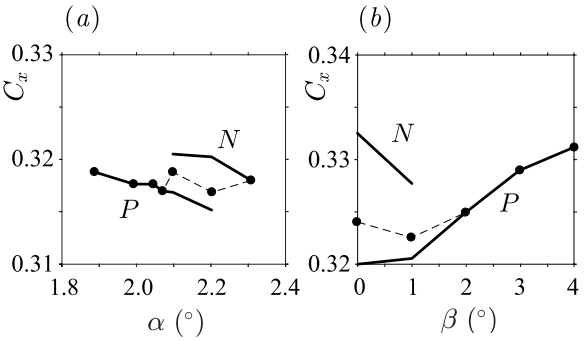

Figure 15: Mean drag coefficient C_x (filled black circles) and conditional averaging based on the sign (N negative and P positive) of the vertical pressure gradient (thick lines) for the Berlingo with closed air-intake in pitch variations and the Partner with closed air-intake in yaw variations.

cially at high driving speeds. The purpose of this section is then to manipulate the wake when in state N in order to retrieve the more efficient state P by simple geometrical modifications.

The passive flow control devices are two vertical plates at both sides of the base and an additional third plate at the roof as illustrated at the top in figure 16. The length of each plate equals the side length they are associated with and the width is $d^* = 0.2$ (*i.e.* $d = 0.3$ m). The Partner is placed in pitching conditions at $\alpha = 2.3°$ to obtain a permanent P state with open air-intake and a permanent N state with closed air intake. These two states can indeed be identified in the corresponding base pressure distribution given in figure 16(a) for open air-intake and figure 16(d) for closed air-intake. We can see that the N state has a larger base suction ($C_b = 0.192$) than the P state ($C_b = 0.184$) while the drag is decreased by 4.6% by avoiding the airflow through the vehicle. Actually, figures 16(a) and 16(d) depict respectively equivalent situations to the baselines of the Kangoo in table 2 with open air-intake and table 3 with closed air-intake. The placement of the side plates degrades the base suction and the drag for the open air intake configuration in figure 16(b) but produces a permanent P state in figure 16(e) which significantly reduces both the base suction and the drag.

The best definitive passive device is with the additional roof plate where drag remains unchanged for open air intake in figure 16(c) compared to no device at all in figure 16(a) and reduced by 8.3% in figure 16(f) compared to open air intake and no device at all in figure 16(a). Thus, the drag reduction of 4.3% obtained by closing the air intake

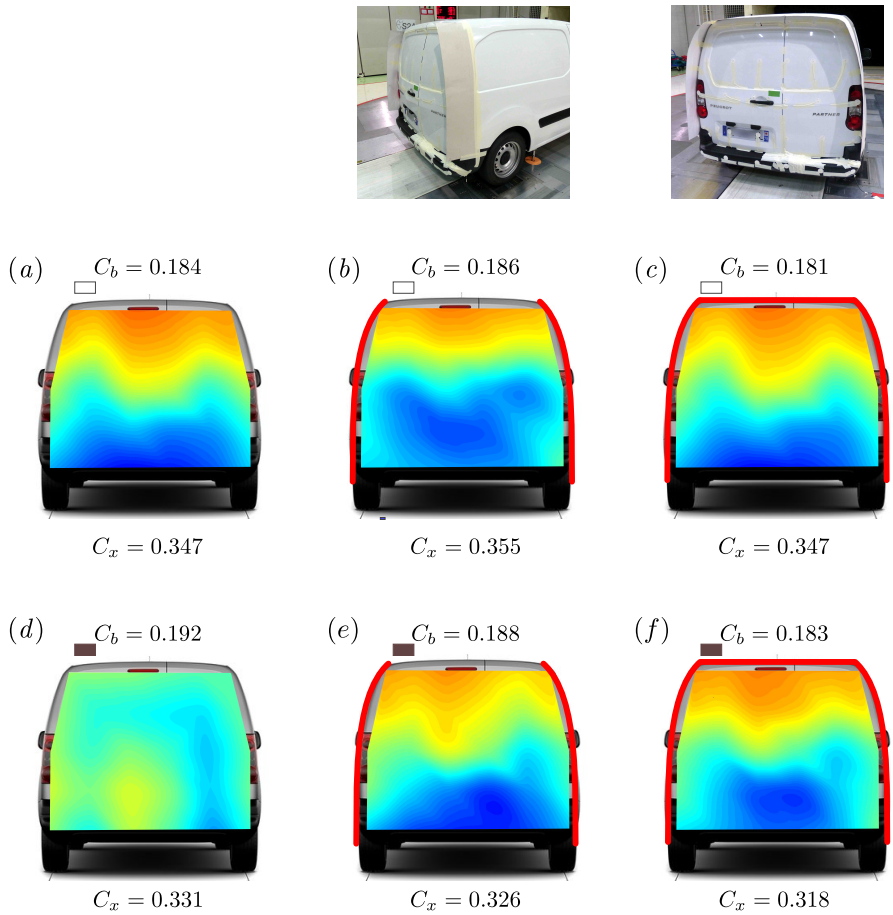

Figure 16: Mean base pressure distribution $C_p(y^*, z^*)$ for the Peugeot Partner at $\Delta\alpha = 2.3°$ and associated mean base suction and drag coefficients C_b and C_x: (a) Open air-intake without control, (b) closed air-intake without control, (c) side plates and closed air-intake, (d) side plates and open air-intake, (e) base cavity and closed air-intake, (f) base cavity and open air-intake. The red lines model the control devices installed on the vehicle.

is improved to 8.3% with an additional passive device controlling the instability without modifying the drag with open air-intake.

4. Discussion and conclusion

The sensitivity analyses of real minivan cars in pitch and yaw reveal the existence of two distinctive opposite and constant values (independent to the car inclination) of the vertical component of the base pressure gradient. They define unambiguously two states of the wake; the P state with positive and the N state with negative pressure gradient. This is in total agreement with flat backed Ahmed bodies [19] and prove that the minivan cars are permanently subjected to the z-instability as characterized by [14]. An important and non trivial consequence is that the vertical asymmetry of the minivan wake as shown in figures 7 and 8 for baseline configurations in real driving conditions is not a consequence of the geometry (car shape, wheels or ground) but to a global steady instability of the wake. The strength of the pressure gradient of the P state is twice that of the N state and produces an additional lift evaluated approximately to $+0.024$ and -0.012 to the basic flow without the instability. For the flat backed Ahmed body in [19] the contribution was evaluated to ± 0.02 because the two states of the z-instability are fairly symmetric despite the proximity of the road and the thin supports. It is likely that the asymmetric global shape of the car and its wide wheels are responsible for the difference in the strength of the P and the N state.

Specific configurations obtained by changing

pitch, yaw, ground clearance and also by closing the air intake, trigger the bistable dynamics from a permanent stable state through a discontinuous transition featuring random exploration of the two states towards the permanent opposite state. By analogy with the y-instability where bistability is a simple consequence of the symmetry restoration operated by developed turbulence, it is likely that these specific configurations are resulting from few asymmetry compensations leading to an effective symmetric configuration. Thus, we believe that the natural geometrical asymmetry can be compensated by a given intensity of the underbody flow at the bottom edge of the base. From all transitions observed in [19] (Ahmed bodies in yaw, pitch and ground clearance variations), in [21] (real Kangoo car in yaw with open and closed air-intake) and in the present paper (real minivans in yaw, pitch and ground clearance variations with open and closed air-intake) we are able to conjecture some rules about the wake state selection. Any modification that reduces the underbody flow intensity is favourable to state P. For initially closed air intake and no yaw, it is achieved by decreasing the ground clearance, pitching down the car, yawing the car and opening the air-intake. If the wake was in state N, then all the mentioned variations could potentially switch the wake to the P state, otherwise the car initially in state P will persist in state P. On the contrary, any modification that increases the underbody flow is favourable to the N state. For initially closed air-intake and no yaw, it is achieved by increasing the ground clearance, and pitching up the car. There is a special case when considering a car with open air-intake in yaw as for the Kangoo car[21]. The resulting underbody flow intensity is not uniquely determine since as the yaw increases less air flows through the car resulting into an increase of the underbody flow while the wake of the leeward wheel tends to decrease the underbody flow. It is likely that for the Kangoo with open air intake the air-intake effect dominate in yaw since a switch from the P to N state operates.

For a given real car configuration, the drag of the N state is larger than that of the P state. One can argue that the higher total lift of the N state (see figures 12, 13), should produce more induced drag than the P state having smaller lift. State P is then preferred for low drag but also for reduced lift associated to better car stability. We have shown that controlling the wake state by selecting a P state with a passive device can lead to important improvement of aerodynamics performances.

The presence of a global instability in the wake offers perspective for flow control and should then be taken into account into future industrial aerodynamics optimization of minivans, but also for SUVs (sport utility vehicles). The control objective can be the state selection as illustrated in the present work, but also the instability suppression that needs further fundamental research.

Acknowledgments

The authors wish to thank Jose Ignacio Jiménez-González for the critical reading of the manuscript and discussions during his stay at ENSTA-ParisTech, The authors are grateful to the *Centre National de Recherche Technologique de Recherche en Aérodynamique et Aéroacoustique des Véhicules terrestres* (CNRT R2A) for funding this work as well as Groupe PSA and Groupe Renault for providing the vehicles. The authors acknowledge the staff of the GIE-S2A for their efficient and continuous support during the test sessions.

References

[1] S. Ahmed, G. Ramm, G. Faitin, Some salient features of the time-averaged ground vehicle wake, SAE Technical Paper Series (1984) 840300.

[2] M. Grandemange, M. Gohlke, O. Cadot, Reflectional symmetry breaking of the separated flow over three-dimensional bluff bodies, Physical Review E 86 (2012) 035302.

[3] M. Grandemange, M. Gohlke, O. Cadot, Turbulent wake past a three-dimensional blunt body. Part 1. Global modes and bi-stability., Journal of Fluid Mechanics 722 (2013) 51–84.

[4] R. Volpe, P. Devinant, A. Kourta, Experimental characterization of the unsteady natural wake of the full-scale square back Ahmed body: flow bi-stability and spectral analysis, Experiments in Fluids 56 (5) (2015) 99.

[5] A. Evrard, O. Cadot, V. Herbert, D. Ricot, R. Vigneron, J. Délery, Fluid force and symmetry breaking modes of a 3D bluff body with a base cavity, Journal of Fluids and Structures 61 (2016) 99–114.

[6] A. Perry, G. Pavia, M. Passmore, Influence of short rear end tapers on the wake of a simplified square-back vehicle: wake topology and rear drag, Experiments in Fluids 57 (11) (2016) 169.

[7] R. Li, D. Barros, J. Borée, O. Cadot, B. R. Noack, L. Cordier, Feedback control of bimodal wake dynamics, Experiments in Fluids 57 (10) (2016) 158.

[8] R. D. Brackston, J. García De La Cruz, A. Wynn, G. Rigas, J. F. Morrison, Stochastic modelling and feedback control of bistability in a turbulent bluff body wake, Journal of Fluid Mechanics 802 (2016) 726749.

[9] E. Varon, Y. Eulalie, S. Edwige, P. Gilotte, J.-L. Aider, Chaotic dynamics of large-scale structures in a turbulent wake, Physical Review Fluids 2 (2017) 034604.

[10] D. Barros, J. Borée, O. Cadot, A. Spohn, B. R. Noack, Forcing symmetry exchanges and flow reversals in turbulent wakes, Journal of Fluid Mechanics 829 (2017) R1.

[11] R. Pasquetti, N. Peres, A penalty model of synthetic micro-jet actuator with application to the control of wake flows, Computers & Fluids 114 (0) (2015) 203–217.

[12] J.-M. Lucas, O. Cadot, V. Herbert, S. Parpais, J. Délery, A numerical investigation of the asymmetric wake mode of a squareback Ahmed body effect of a base cavity., Journal of Fluid Mechanics 831 (1) (2017) 675 – 697.

[13] O. Evstafyeva, A. S. Morgans, L. Dalla Longa, Simulation and feedback control of the Ahmed body flow exhibiting symmetry breaking behaviour, Journal of Fluid Mechanics 817 (2017) R2.

[14] M. Grandemange, M. Gohlke, O. Cadot, Bi-stability in the turbulent wake past parallelepiped bodies with various aspect ratios and wall effects, Physics of Fluids 25 (2013) 95–103.

[15] M. Grandemange, O. Cadot, A. Courbois, V. Herbert, D. Ricot, T. Ruiz, R. Vigneron, A study of wake effects on the drag of the Ahmed squareback model at the industrial scale, Journal of Wind Engineering and Industrial Aerodynamics 145 (2015) 282–291.

[16] O. Cadot, A. Evrard, L. Pastur, Imperfect supercritical bifurcation in a three-dimensional turbulent wake, Physical Review E 91 (6) (2015) 063005.

[17] T. Castelain, M. Michard, M. Szmigiel, D. Chacaton, D. Juvé, Identification of flow classes in the wake of a simplified truck model depending on the underbody velocity, Journal of Wind Engineering and Industrial Aerodynamics 175 (2018) 352–363.

[18] H.-J. Schmidt, R. Woszidlo, C. N. Nayeri, C. O. Paschereit, The effect of flow control on the wake dynamics of a rectangular bluff body in ground proximity, Experiments in Fluids 59 (6) (2018) 107.

[19] G. Bonnavion, O. Cadot, Unstable wake dynamics of rectangular flat-backed bluff bodies with inclination and ground proximity, Journal of Fluid Mechanics 854 (2018) 196–232.

[20] O. Cadot, A. Courbois, D. Ricot, T. Ruiz, F. Harambat, V. Herbert, R. Vigneron, J. Délery, Characterisations of force and pressure fluctuations of real vehicles, Int. J. Engineering Systems Modelling and Simulation 8 (2) (2016) 99–105.

[21] G. Bonnavion, O. Cadot, A. Évrard, V. Herbert, S. Parpais, R. Vigneron, J. Délery, On multistabilities of real car's wake, Journal of Wind Engineering and Industrial Aerodynamics 164 (2017) 22–33.

[22] P. Waudby-Smith, T. Bender, R. Vigneron, The GIE S2A full-scale aeroacoustic wind tunnel, SAE Technical Paper Series (2004) 010808.

[23] M. Grandemange, M. Gohlke, O. Cadot, Turbulent wake past a three-dimensional blunt body. Part 2. Experimental sensitivity analysis., Journal of Fluid Mechanics 752 (2014) 439–461.